

Short Communication

Improvement of Resistance to Hydrogen Embrittlement for 1300MPa Ultra-high Strength Steel by Introducing Nano-sized Cu-rich Phase Precipitation

Chengning Li^{1,2,*}, Heshan Gao^{1,2}, Yuanbo Jiang^{1,2}, Wen Fu^{1,2}, Qiangjun Yan^{1,3}, Wenyi Hu⁴, Dongpo Wang^{1,2}, Xinjie Di^{1,2,*}

¹ School of Materials Science and Engineering, Tianjin University, Tianjin, 300350, China

² Tianjin Key Laboratory of Advanced Joining Technology, Tianjin, 300350, China

³ Nanjing Iron & Steel Co., Ltd, Jiangsu Nanjing, 210035, China

⁴ College of Chemistry & Materials Science, Longyan University, Fujian Longyan, 364012, China

*E-mail: licn@tju.edu.cn, dixinjie@tju.edu.cn

Received: 2 March 2022/ Accepted: 14 April 2022/ Published: 7 May 2022

Cu-bearing and conventional martensite ultra-high strength steels with tensile strengths of 1300 MPa were investigated to explore the effect of the precipitation of Cu-rich particles on hydrogen embrittlement (HE). The results showed that the Cu-bearing steel strengthened by 9R Cu-rich precipitates had nanoscale and coherent properties and exhibited a higher resistance to HE than the conventional martensite steel. The Cu-rich precipitates served as irreversible hydrogen traps, leading to a low diffusible hydrogen content and hydrogen diffusivity for the Cu-bearing steel, thereby providing an effective approach to improve the hydrogen embrittlement of ultra-high strength steels.

Keywords: Hydrogen embrittlement; Ultra-high strength steel; Cu-rich precipitation; Thermal desorption spectrometry

1. INTRODUCTION

As the strength of steel increases, so does the susceptibility to hydrogen embrittlement (HE), which can be destructive to steel structures [1, 2]. Over the past two decades, the precipitation of Cu-particles in low carbon steel has been used to obtain high strength and good weldability [3, 4]. Jiao [5] reported that Cu-rich nanoprecipitates can increase the yield strength of high-strength steels by 140 MPa via solid-solution strengthening, grain refinement strengthening and precipitation strengthening. Cu-rich precipitates evolve by aging treatment as follows: precipitates with B2-ordered structures are transformed successively into metastable 9R structures, metastable 3R structures, and finally stable FCC structures [3, 6]. The precipitation of Cu-rich particles in high-strength steels has also been found to increase the resistance to HE due to the action of irreversible hydrogen traps. Shi [7] proved that Cu-rich

precipitates with diameters of 10~20 nm improved the resistance of high-strength pipeline steels to hydrogen-induced cracks (HICs). Yoo [8] reported that the addition of 3 wt.% Cu to austenite-ferrite duplex steel increased the HE resistance and proposed that Cu-rich particles with B2 structures and diameters of 200~600 nm could reduce the hydrogen diffusivity. Lin [9] reported that FCC Cu-rich particles have an enhanced capacity for hydrogen trapping and higher resistance to hydrogen embrittlement than TiC platelets and grain boundaries in tempered martensitic steels. In recent years, Cu-bearing ultra-high strength steels with tensile strengths higher than 1000 MPa have been developed and studied. Li. [10] reported that Cu-rich multistructured precipitates containing B2-ordered structures and transitional structures between B2-ordered and 9R structures increased the strength of ultra-high strength steel. Fu [11] reported that the precipitation of 9R-structured Cu-rich particles in ultra-high strength steel resulted in good matching of strength and toughness. It is well known that ultra-high strength steels are susceptible to HE, especially for steels with tensile strengths higher than 1200 MPa [1]. It remains to be determined whether the precipitation of 9R-structured Cu-rich nanoparticles can alleviate HE.

We carried out 9R-structured Cu-rich precipitation to obtain 1300 MPa ultra-high strength steels with satisfactory toughness [11]. It has been proposed that Cu-rich precipitates can act as irreversible hydrogen traps, which may alleviate HE for ultra-high strength steel. However, few studies have demonstrated the effect of 9R-structured nanosized Cu-rich precipitation on HE of ultra-high strength steel. In the present study, we demonstrated the difference between the resistances to HE for Cu-bearing and conventional martensite ultra-high strength steels and explored the effect mechanism of nanosized Cu-rich precipitation on HE. Hydrogen-induced degradation of the ductility of ultra-high strength steel was investigated using electrochemical hydrogen charging, tensile tests, and hydrogen-induced cracks. The mechanism of the resistance of the ultra-high strength steels to HE was analyzed by observation of fractographic morphologies, hydrogen trapping states and the hydrogen diffusion coefficient.

2. EXPERIMENTAL PROCEDURE

2.1. Materials

As-received Cu-bearing and conventional martensite steel casting ingots were reheated to 1373 K for 2 h, hot-rolled to a thickness of 12 mm and directly quenched. The Cu-bearing steel was tempered for 2 h at 823 K to precipitate Cu-rich particles, and the conventional martensite steel was tempered at 473 K for 1 h to balance strength and toughness. The chemical compositions of the Cu-bearing and conventional martensite steels are listed in Table 1.

Table 1. Chemical composition of the experimental steels

Chemical composition (wt.%)	C	Si	Mn	Cu	Ni	Mo	Cr	Nb	Ti	Al
Cu-bearing steel	0.056	0.48	1.02	2.2	4.1	/	/	0.07	0.02	0.72
Conventional martensite steel	0.16	0.28	0.94	/	1.2	0.8	0.42	0.03	0.015	0.049

2.2. Microstructural characterization

The microstructure of the steels was characterized by X-ray diffractometry (XRD), and the results were used to calculate the dislocation density. The samples were prepared for XRD analysis by mechanical polishing with silicon carbide paper. The diffraction profiles of the (110), (200), (211), (220) and (310) reflections were measured at a speed of 1.5°/min over the 2θ range of 30-120° using a conventional diffractometer operating at 40 kV and 40 mA. The dislocation density was calculated by the MWH equation [12]:

$$\Delta K \cong \frac{0.9}{D} + bM\sqrt{\frac{\pi\rho}{2}} \left(K\bar{c}^{\frac{1}{2}} \right) \quad (1)$$

where ΔK is the full width at half maximum, b is the Burgers vector, ρ is the dislocation density, D is a size parameter, M is a constant that depends on the effective outer cutoff radius of dislocations and \bar{c} is the average contrast coefficient for dislocations for different reflections.

The microstructure of the steels was characterized by field emission electron microscopy (FE-SEM, JSM-7800F). The martensite laths of the experimental steels and the Cu-rich precipitates of the Cu-bearing steel were investigated using transmission electron microscopy (TEM, JEM-2100). Thin foils for TEM were prepared by cutting slices of the steels, followed by grinding to 500–50-μm thicknesses using silicon-carbide papers and jet electropolishing using a mixed solution of 10% perchloric acid and 90% absolute ethyl alcohol at -40 °C.

2.3. Tensile tests on precharged steels and tests on hydrogen-induced cracks

Standard cylindrical tensile test specimens with a 25.0-mm gauge length and a 6.25-mm diameter were prepared according to ASTM A370 to test the normal tensile properties of the steels. To test the resistance of the steels to HE, tensile specimens with gauge dimensions of 25×6.25×1.5 mm were prepared. Before performing the tensile test, the specimens were electrochemically precharged in a solution of 0.01 mol/L H₂SO₄ and 3 g/L NH₄SCN at a current density of 15 mA/cm² for 1 h or 2 h. The sample acted as the cathode, and the platinum electrode acted as the anode. A computerized MTS machine was used to perform an instantaneous tensile test at a displacement rate of 0.12 mm/min. The HE susceptibility was evaluated by the loss of tensile elongation (El_{loss}), which is defined below[8]:

$$El_{loss} = \frac{El_{uncharged} - El_{charged}}{El_{uncharged}} \times 100\% \quad (1)$$

where $El_{uncharged}$ and $El_{charged}$ are the fracture strains with and without hydrogen charging, respectively.

To evaluate the HIC susceptibility under extreme conditions, specimens with dimensions of 10.5×10.5×6 mm were also electrochemically charged using a mixed solution of 0.5 mol/L H₂SO₄ and 3 g/L NH₄SCN for 72 h at a current density of 100 mA/cm². The macroscopic morphology of the HICs were characterized by a super-depth-of-field microscope (Smart Zoom 5). Based on the NACE TMO284 standard, the crack length ratio (CLR), crack thickness ratio (CTR) and crack sensibility ratio (CSR) were calculated as follows[13]:

$$CLR = \frac{\sum a}{W} \times 100\% \quad (2)$$

$$CTR = \frac{\sum b}{T} \times 100\% \quad (3)$$

$$CSR = \frac{\Sigma(a \times b)}{W \times T} \times 100\% \quad (4)$$

where a is the crack length (mm), b is the crack thickness (mm), W is the sample width, and T is the sample thickness.

2.4. Electrochemical permeation tests

Hydrogen permeation tests were performed to determine the hydrogen diffusivity. Plate-type specimens with dimensions of 10×10×1.5 mm were charged in a hydrogen-oxidant solution (0.1 M NaOH) contained in charging (0.01 mol/L H₂SO₄ + 3 g/L NH₄SCN) cells. One side of the oxidized specimen was electroplated with Ni for 5 min to prevent oxide formation during the test. The data obtained from the hydrogen permeation tests were used to determine the effective diffusivity (D_{eff}) [8]:

$$D_{eff} = \frac{L^2}{T_{lag}} \quad (5)$$

where L is the specimen thickness and T_{lag} is the time lag for a transient current density that is 0.63 times the steady-state current density (I_{ss}).

2.5. Hydrogen-charging process and thermal desorption analysis

The specimen dimensions along the rolling direction were 25×6.25×1.5 mm. Before being subjected to hydrogen charging, the specimens were polished using 2000-grit silicon-carbide papers to remove the oxide layer. Electrochemical hydrogen charging was conducted using a mixed solution of 0.01 mol/L H₂SO₄ + 3 g/L NH₄SCN at room temperature for 1 h. A current density of 15 mA/cm² was used for hydrogen charging.

After the hydrogen-charging experiments were completed, thermal desorption analysis (TDA) was conducted using a quadrupole mass spectrometer to investigate the hydrogen desorption behavior of the experimental steels. The specimens were heated from 25 to 750 °C using a tube furnace at a heating rate of 100 °C/h. The TDA results were used to estimate the diffusible and nondiffusible hydrogen contents of the experimental steels under electrochemical precharging.

3. RESULTS

3.1 Microstructural features and mechanical properties of ultra-high strength steels

Only the BCC phase was found in both the Cu-bearing and conventional martensite steels, as shown in Figure 1. The dislocation densities of the Cu-bearing and conventional steels were $2.3 \times 10^{13} \text{ m}^{-2}$ and $8.1 \times 10^{13} \text{ m}^{-2}$, respectively.

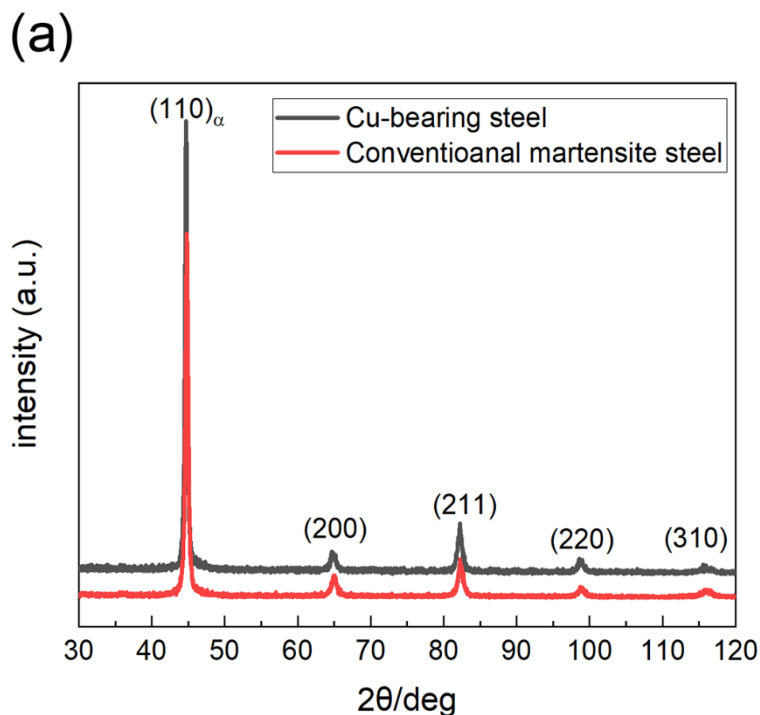


Figure 1. X-ray diffractograms of Cu-bearing and conventional martensite steels.

Figure 2 presents the SEM morphologies of the conventional martensite and Cu-bearing steels. The microstructure of the conventional martensite steel corresponded to that of lath martensite, whereas the Cu-bearing steel consisted of lath martensite and a small quantity of bainite.

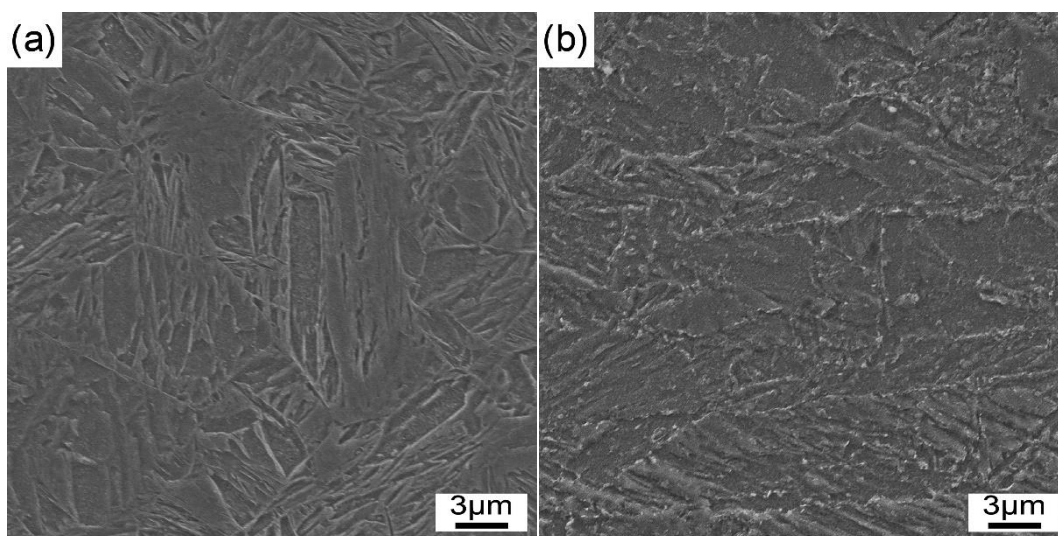


Figure 2. SEM morphologies of (a) conventional martensite and (b) Cu-bearing steels.

Figure 3 presents transmission electron microscopy images of the conventional martensite and Cu-bearing steels. Figure 3a shows lath martensite and no precipitation in the conventional martensite

steel. Compared with the conventional martensite steel, the martensite in the Cu-bearing steel had a larger lath size (as shown in Figure 3b), which may be attributed to the high tempering temperature used. A high density of precipitates with sizes of 9-15 nm was observed in the tempered martensite matrix, as presented in Figure 3c. The EDS results showed that these precipitates consisted of Fe, Cu, and Ni. Figure 3d shows a high-resolution TEM image and fast Fourier transform taken along the [111] zone axis, which indicated a 9R structure for the Cu-rich precipitates. The degree of mismatch between 9R-Cu and α -Fe was $\sim 4.8\%$, indicating coherent boundaries between these phases.

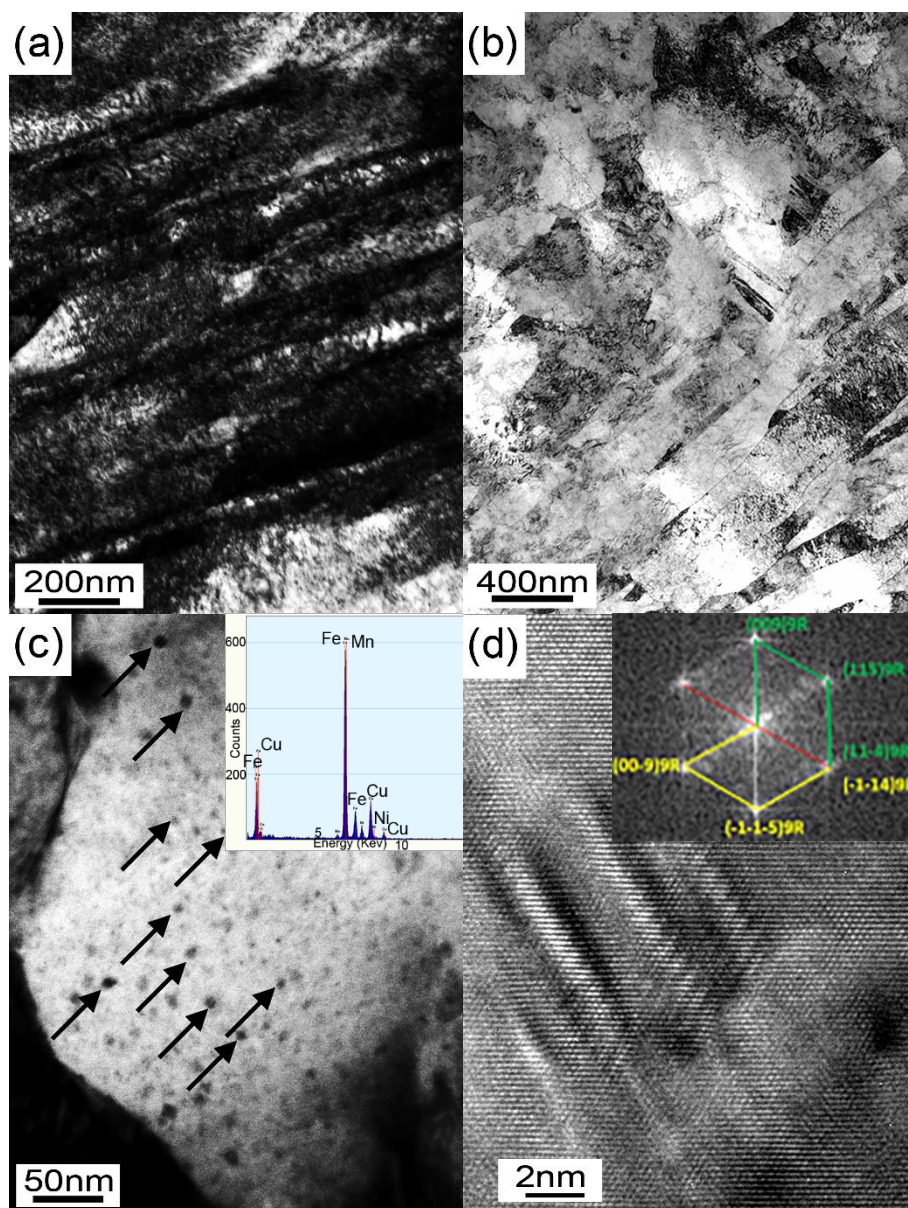


Figure 3. TEM of (a) conventional martensite and (b) Cu-bearing steels, (c) morphology and EDS results of the precipitates in the Cu-bearing steel, and (d) HRTEM image and FFT of the precipitates in the Cu-bearing steel.

Figure 4 shows the engineering tensile stress–strain curves of the conventional martensite and Cu-bearing steels. The yield strength, tensile strength and elongation of the conventional martensite steel were 1147 MPa, 1429 MPa and 17.17%, respectively. The yield strength, tensile strength and elongation of the Cu-bearing steel were 1270 MPa, 1277 MPa and 15.23%, respectively. The average impact absorbed energy at $-40\text{ }^{\circ}\text{C}$ of the conventional martensite and Cu-bearing steels was 81.5 J and 44.2 J, respectively.

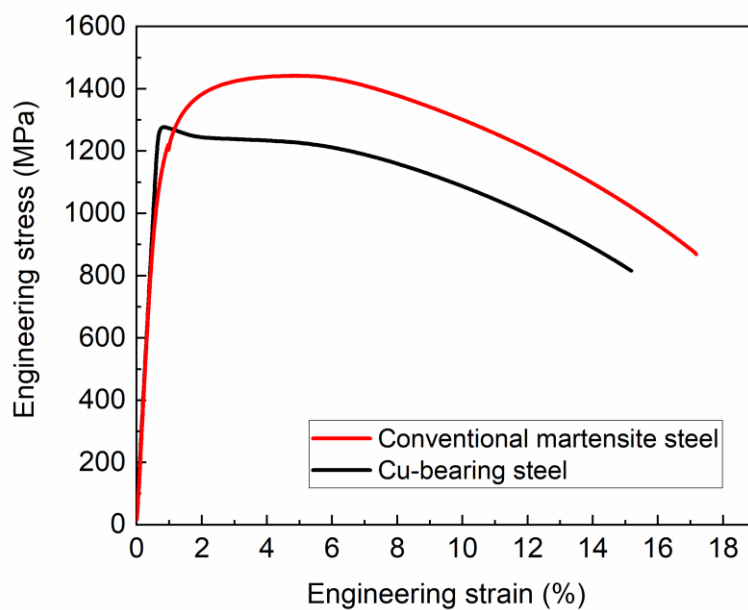


Figure 4. Engineering tensile stress–strain curves of the conventional martensite and Cu-bearing steels.

3.2 Hydrogen-induced cracks and hydrogen embrittlement susceptibility

Figure 5 presents the engineering stress–strain curves of the experimental steels before and after hydrogen charging. Precharging the conventional martensite steel for 1 h caused the elongation to decrease from 9.15% to 4.19%, with an $E_{l_{\text{loss}}}$ of 54.2%. Precharging the Cu-bearing steel for 1 h caused the elongation to decrease from 7.94% to 6.51%, corresponding to an $E_{l_{\text{loss}}}$ of only 18.1%. Extending the hydrogen precharging time to 2 h resulted in an abrupt loss of the load-bearing capacity of the conventional martensite steel, whereby the breaking strength dropped to only 479 MPa. By comparison, the Cu-bearing steel had a higher breaking strength of 614 MPa.

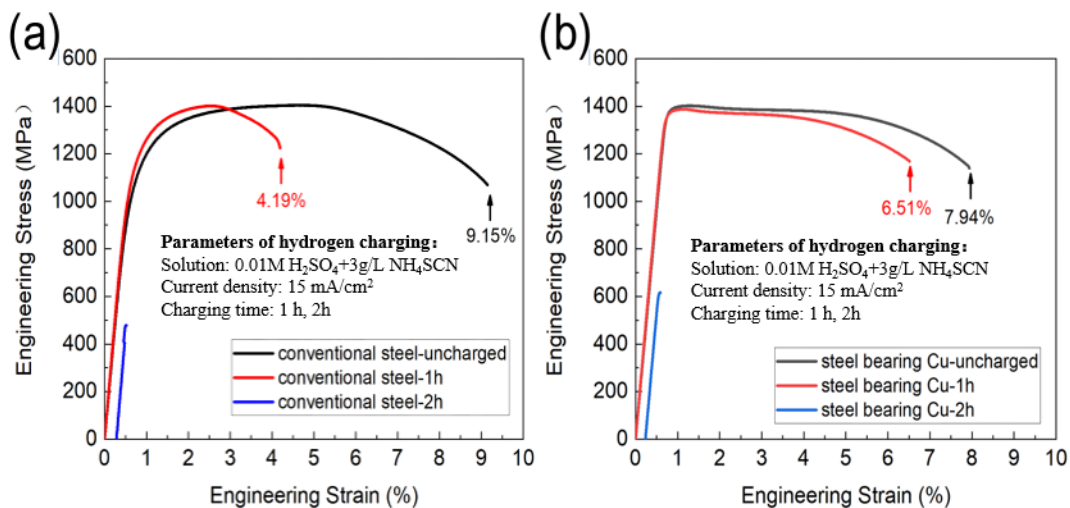


Figure 5. Engineering tensile stress–strain curves in the presence and absence of hydrogen for (a) conventional martensite and (b) Cu-bearing steels.

Figure 6 presents the macroscopic morphology of the HICs for the conventional martensite and Cu-bearing steels. The two steels exhibit clearly different resistances to HIC under the hostile hydrogen environment. For conventional martensite steel, the CTR, CLR and CSR are 63.5%, 54.7% and 34.7%, respectively. However, there are no cracks in the Cu-bearing steel. In contrast to the results obtained for the Cu-bearing steel, the surface of the conventional martensite steel contained numerous HICs under extreme conditions, which demonstrated this steel was prone to form HICs. Thus, the resistance to HE of the Cu-bearing steel was indeed enhanced over that of the conventional martensite steel.

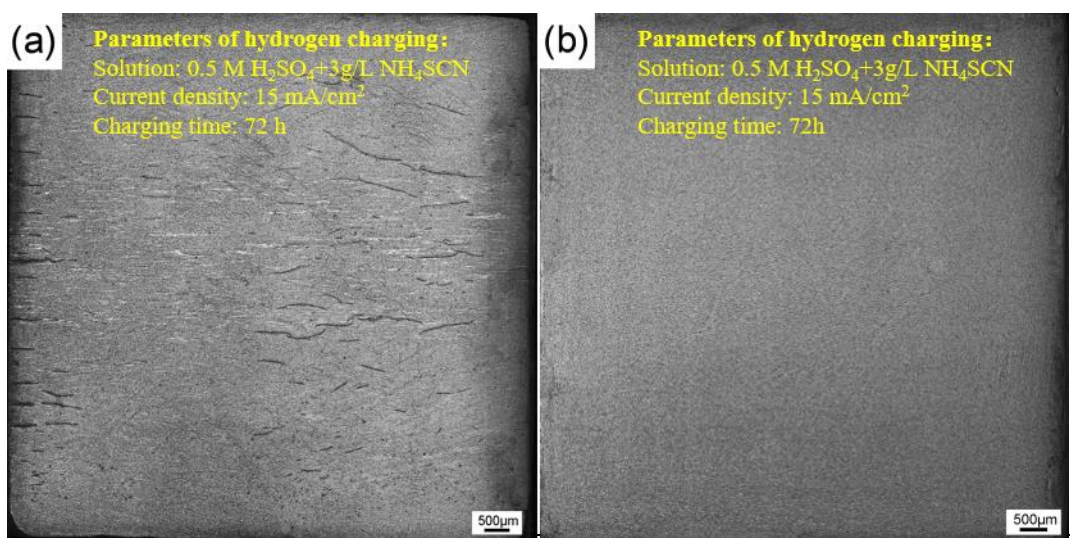


Figure 6. The macroscopic morphology of HICs for (a) conventional martensite and (b) Cu-bearing steels.

3.3. Fractographic morphologies

Figures 7-9 show SEM images of the fracture surfaces of the experimental steels. Figure 7 shows that the uncharged experimental steels have ductile fracture surfaces with fine dimples. Figure 8 presents the fracture surfaces of these two steels after 1 h of hydrogen charging.

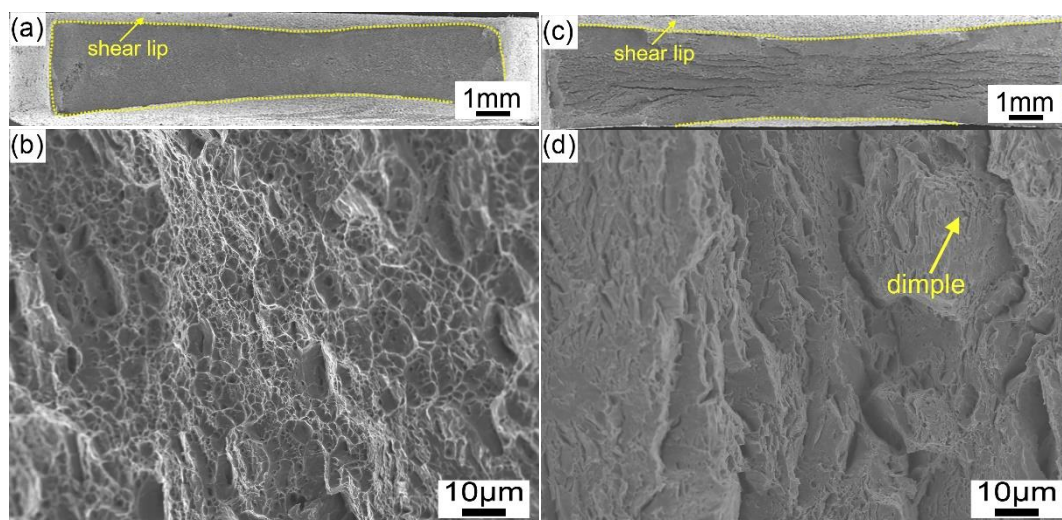


Figure 7. SEM images of fracture surfaces of uncharged experimental steels: (a) and (b) conventional martensite steel and (c) and (d) Cu-bearing steel.

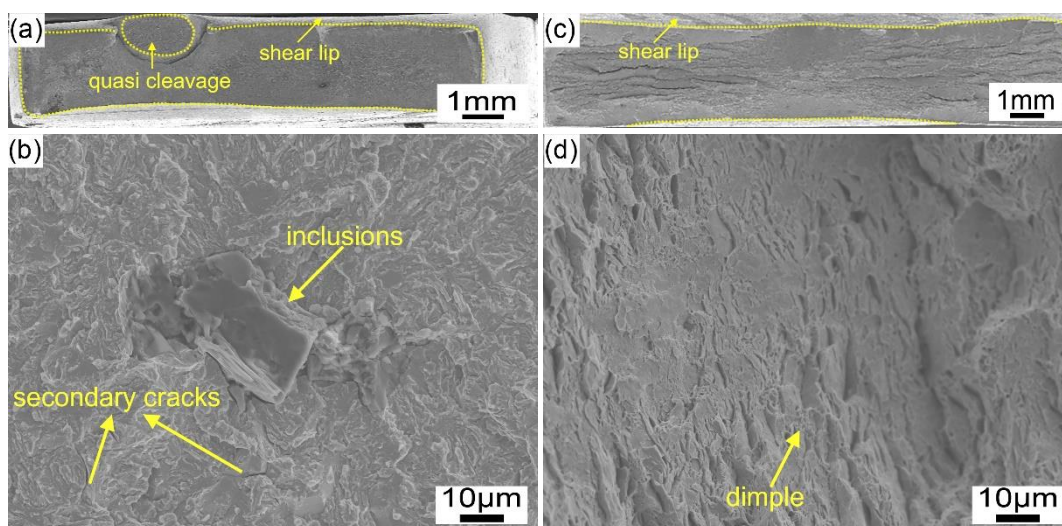


Figure 8. SEM images of fracture surfaces of experimental steels after 1 h of hydrogen charging: (a) and (b) conventional martensite steel and (c) and (d) Cu-bearing steel.

The shear-lip area of the fracture is lower after hydrogen charging than before hydrogen charging for the conventional martensite and Cu-bearing steels. A characteristic mixed quasi-cleavage river-pattern and dimple-like fracture surface was observed for the conventional martensite steel, as shown in Figure 8a-b. In Figure 8c-d, the fractographic morphology of the Cu-bearing steel contains dimples.

However, the fracture surface of the charged steel is flatter than that of the uncharged steel. Figure 9 shows the fractographies of the experimental steels after 2 h of hydrogen charging. Both experimental steels exhibit a quasi-cleavage fracture pattern. The secondary cracks that can be observed in the conventional martensite steel indicate very severe hydrogen-induced damage resulting from the extended hydrogen-charging time.

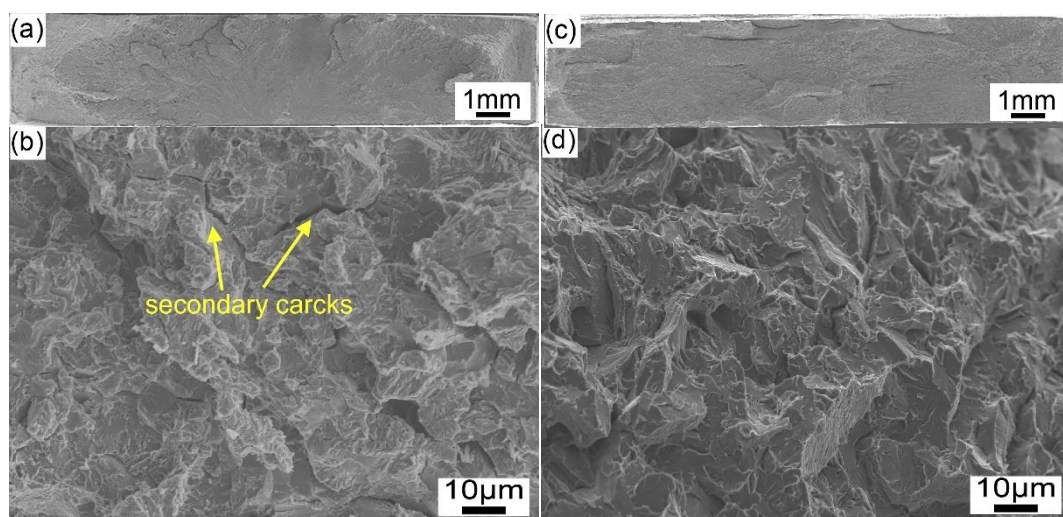


Figure 9. SEM images of fracture surfaces of the experimental steels subjected to 2 h of hydrogen charging: (a)-(b) conventional martensite steel and (c)-(d) Cu-bearing steel.

4. DISCUSSION

4.1 Effect of Cu-rich precipitation on hydrogen trapping states

Figure 10 shows typical hydrogen desorption curves for the precharged steels. The curves of both experimental steels exhibit a peak corresponding to reversible hydrogen trapping, showing that hydrogen atoms are desorbed below 300 °C [14, 15]. Hydrogen was desorbed from the conventional martensite steel upon increasing the temperature to 323–457 K, and the hydrogen desorption curve exhibited a peak at 390 K. The hydrogen desorbed in this temperature range was identified as diffusible hydrogen [14, 15], which was measured at a content of 1.074 ppm by TDS and considered to be the direct cause of HE. A considerably smaller diffusible hydrogen desorption peak was observed at 390 K in the curve of the Cu-bearing steel, and the corresponding hydrogen content was only 0.491 ppm. The hydrogen content of the reversible hydrogen traps for the conventional martensite steel was twice as large as that for the Cu-bearing steel. As dislocations act as rapid and efficient carriers of hydrogen [2], the significant decrease in the dislocation density for the Cu-bearing steel compared to that of the conventional martensite steel inhibited hydrogen diffusion and reduced the diffusible hydrogen content. Interestingly, the hydrogen desorption curve of the Cu-bearing steel exhibited a second hydrogen desorption peak at ~690 K, and the corresponding hydrogen content was 0.125 ppm, which was attributed to the presence

of irreversible hydrogen traps. Yoo [8] reported irreversible hydrogen trapping sites in a lightweight steel containing 3 wt.% Cu. Lin [16] reported an activation energy of 35 KJ/mol for the formation of nanometer-sized Cu-rich precipitates in a martensitic steel containing 1.2 wt.% Cu, and there was no discernible peak in the hydrogen desorption curve corresponding to irreversible hydrogen trapping sites. This condition is attributed to the 1.2 wt.% Cu content of the Cu-bearing steel, which is sufficient to create irreversible hydrogen trapping sites. Kaneko [17] reported that irreversible traps are more efficient at trapping hydrogen than reversible traps. During hydrogen charging of the experimental steels, hydrogen was first trapped at the irreversible trap sites and then at the reversible trap sites. Thus, the hydrogen content of the reversible traps decreased in the presence of the irreversible traps.

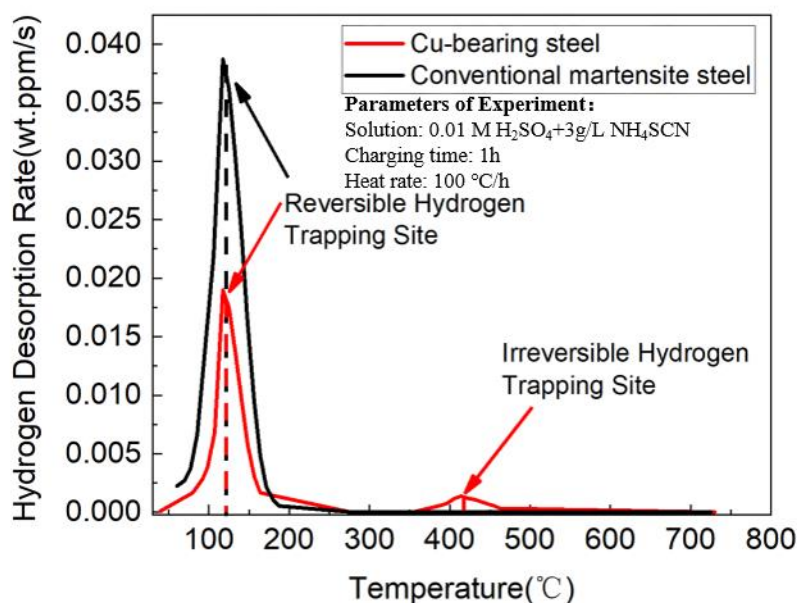


Figure 10. TDA curves for conventional martensite and Cu-bearing steels after 1 h of hydrogen charging.

4.2 Mechanism of resistance to HE for Cu-rich-precipitation-strengthened ultra-high strength steel

Figure 5 shows that the ductility of both the conventional martensite and Cu-bearing steels were degraded in the presence of hydrogen. Figure 8a-b shows the fracture morphology of conventional martensite steel after 1 h of hydrogen charging, where hydrogen-induced microsecondary cracks occur next to the inclusions, finally resulting in quasi-cleavage fracture. Hydrogen diffused into the materials and accumulated at the inclusions, thereby inducing a pressure. When hydrogen-induced pressure exceeds the matrix strength, HIC occurs in the steels. In Figure 8c-d, the fracture morphology of the Cu-bearing steel after 1 h of hydrogen charging indicates ductile fracture with dimples. This phenomenon is related to hydrogen-induced nucleation and coalescence of microvoids [18, 19]. Hydrogen in steels promotes the nucleation, growth, and interconnection of vacancies, which eventually results in ductile fracture under tensile stress. Hydrogen charging for 2 h results in a sufficiently high hydrogen content in the steels to induce a pressure that exceeds the matrix strength, whereby secondary cracks are

generated in the steels. Furthermore, when the H-charged specimens are plastically deformed, dislocations increase the hydrogen diffusivity by accelerating the motion of hydrogen atoms. Thus, cleavage fracture occurs throughout the sample for the conventional martensite and Cu-bearing steels.

The first reason that the Cu-bearing steel has a higher resistance to HE than the conventional martensite steel is that the hydrogen diffusivity is lower. Figure 11 shows the results of hydrogen permeation tests conducted on the conventional martensite and Cu-bearing steels to measure the hydrogen diffusivity. The hydrogen permeation curve of the Cu-bearing steel is shifted downwards and to the right of the corresponding curve for the conventional martensite steel, showing that the time for hydrogen to diffuse through the entire specimen was longer for the Cu-bearing steel, which therefore had a lower permeation capability. The measured D_{eff} of the conventional martensite steel was 1.19×10^{-10} m²/sec, whereas that of the Cu-bearing steel was only 8.69×10^{-11} m²/sec. Compared to the results for the conventional martensite steel, the lower hydrogen diffusivity of the Cu-bearing steel was the main factor that enhanced the resistance to hydrogen embrittlement. A low hydrogen diffusivity can reduce the depth of hydrogen permeation in steels and prevent accumulation of hydrogen atoms at defects, which can reduce hydrogen-induced cracking caused by excessive local hydrogen pressure.

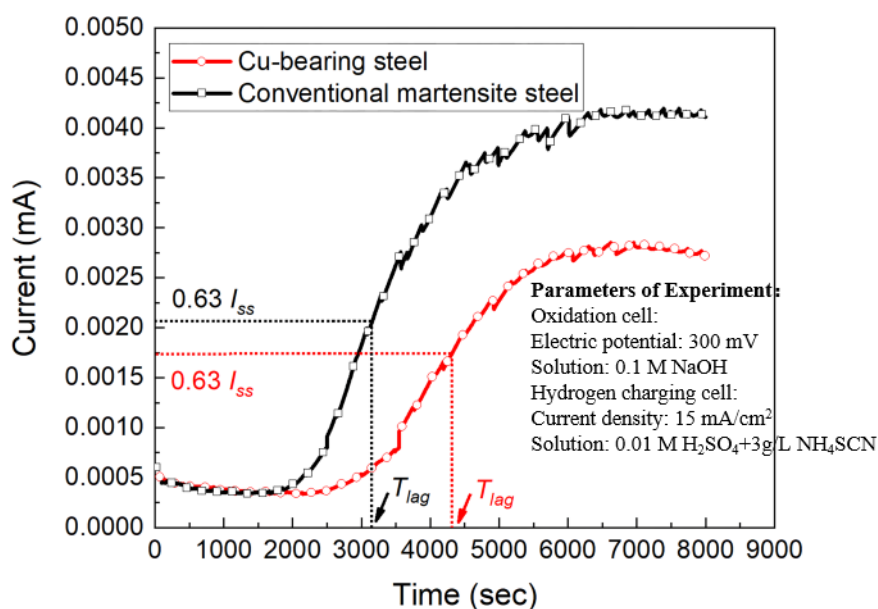


Figure 11. Time-dependent permeation current curves for the conventional martensite and Cu-bearing steels.

The second reason that the Cu-bearing steel has a higher resistance to HE than the conventional martensite steel is the presence of 9R-structured Cu-rich precipitates. It is well established that precipitates, such as TiC, NbC, VC and Fe₃C particles, can act as irreversible hydrogen traps, especially nanosized coherent or semicoherent particles [2, 8, 20]. Therefore, the irreversible hydrogen traps in the Cu-bearing steel were identified as coherent Cu-rich nanoparticles. A low energy barrier for hydrogen trapping at the coherent particle/matrix interface [21] could facilitate hydrogen trapping by Cu-rich nanoparticles, leading to a reduction in the hydrogen diffusivity and preventing HE [8]. These hypotheses

were used to identify the Cu-rich nanoparticles in the experimental steel as effective irreversible hydrogen traps. In addition, Yoo [8] reported that the precipitation of Cu-rich particles at grain boundaries created reversible sites, thereby resulting in a transition from reversible to irreversible sites. Therefore, the effect of the irreversible traps and the transition from reversible to reversible sites induced by the precipitation of Cu-rich nanoparticles further decreased the hydrogen diffusivity and susceptibility to HE.

4. CONCLUSIONS

A Cu-bearing steel strengthened by nanosized coherent 9R Cu precipitates exhibited no hydrogen-induced cracks and a small elongation loss of 18.1% under the experimental conditions investigated, whereas a conventional martensite steel exhibited numerous cracks and a high elongation loss of 54.2%, indicating the Cu-bearing steel exhibited a higher resistance to hydrogen embrittlement than the conventional martensite steel. The enhanced resistance to hydrogen embrittlement of the Cu-bearing steel was attributed to a lower content of diffusible hydrogen and hydrogen diffusivity compared to the conventional martensite steel resulting from the formation of Cu-rich precipitates and an accompanying reduction in the dislocation density.

ACKNOWLEDGEMENTS

This study was financially supported by the Tianjin Natural Science Foundation (grant No. 19JCQNJC02100), National Natural Science Foundation of China (grant Nos. 51804217 and 52074191).

References

1. M.C. Jo, J. Yoo, S. Kim, S. Kim, J. Oh, J. Bian, S.S. Sohn and S. Lee, *Mater. Sci. Eng., A*, 789 (2020) 139656.
2. J. Yoo, M.C. Jo, M.C. Jo, S. Kim, J. Oh, J. Bian, S.S. Sohn and S. Lee, *Mater. Sci. Eng., A*, 791 (2020) 139763.
3. Z.B. Jiao, J.H. Luan, M.K. Miller and C.T. Liu, *Acta Mater.*, 97 (2015) 58.
4. D. Isheim, M.S. Gagliano, M.E. Fine and D.N. Seidman, *Acta Mater.*, 54 (3) (2006) 841.
5. Z.B. Jiao, J.H. Luan, Z.W. Zhang, M.K. Miller, W.B. Ma and C.T. Liu, *Acta Mater.*, 61 (16) (2013) 5996.
6. Y.U. Heo, Y.K. Kim, J.S. Kim and J.K. Kim, *Acta Mater.*, 61 (2) (2013) 519.
7. X. Shi, W. Yan, W. Wang, Y. Shan and K. Yang, *Mater. Des.*, 92 (2016) 300.
8. J. Yoo, M.C. Jo, D.W. Kim, H. Song, M. Koo, S.S. Sohn and S. Lee, *Acta Mater.*, 196 (2020) 370.
9. Y.C. Lin, I.E. McCarroll, Y.T. Lin, W.C. Chung, J.M. Cairney and H.W. Yen, *Acta Mater.*, 196 (2020) 516.
10. C. Li, R. Duan, W. Fu, H. Gao, D. Wang and X. Di, *Mater. Sci. Eng., A*, 817 (2021) 141337.
11. W. Fu, C. Li, R. Duan, H. Gao, X. Di and D. Wang, *Mater. Sci. Eng., A*, 833 (2022) 142567.
12. J. Pešička, R. Kužel, A. Dronhofer and G. Eggeler, *Acta Mater.*, 51 (16) (2003) 4847.
13. S. Zhang, E. Fan, J. Wan, J. Liu, Y. Huang and X. Li, *Corros. Sci.*, 139 (2018) 83.
14. S.K. Dwivedi and M. Vishwakarma, *Int. J. Hydrogen Energy*, 43 (46) (2018) 21603.
15. S.S. Sohn, H. Song, J.G. Kim, J.-H. Kwak, H.S. Kim and S. Lee, *Metall. Mater. Trans. A*, 47 (2)

(2015) 706.

16. Y.C. Lin, D. Chen, M.H. Chiang, G.J. Cheng, H.C. Lin and H.W. Yen, *JOM*, 71 (4) (2019) 1349.
17. M. Kaneko, T. Doshida and K. Takai, *Mater. Sci. Eng., A*, 674 (2016) 375.
18. G. Lv, M. Zhang, H. Zhang and Y. Su, *Int. J. Hydrogen Energy*, 43 (32) (2018) 15378.
19. D. Ahn, P. Sofronis and R. Doddsjr, *Int. J. Hydrogen Energy*, 32 (16) (2007) 3734.
20. S. Zhang, J. Wan, Q. Zhao, J. Liu, F. Huang, Y. Huang and X. Li, *Corros. Sci.*, 164 (2020) 108345.
21. F.G. Wei and K. Tsuzaki, *Metall. Mater. Trans. A*, 37 (2006) 331.

© 2022 The Authors. Published by ESG (www.electrochemsci.org). This article is an open access article distributed under the terms and conditions of the Creative Commons Attribution license (<http://creativecommons.org/licenses/by/4.0/>).